Review

The AMSR-E NT2 Sea Ice Concentration Algorithm : its Basis and Implementation

Thorsten Markus* and Donald J. Cavalieri*

Abstract

The U.S. AMSR-E Science Team uses the enhanced NASA Team (NT2) sea ice concentration algorithm to calculate the standard Arctic and Antarctic sea ice concentration products. The NT2 algorithm significantly reduces the problem of a low ice concentration bias associated with surface effects apparent in sea ice retrievals from areas of deep snow using the original NASA Team (NT) algorithm. This enhancement is achieved through the use of the AMSR-E 89 GHz channels. The NT2 accommodates ice temperature variability through the use of radiance ratios as in the original NT algorithm and has the added advantage of providing weather-corrected sea ice concentrations through the utilization of a forward atmospheric radiative transfer model. This paper gives a brief summary of the concept of the algorithm and provides details of its implementation as part of the routine U.S. AMSR-E Science Team data product generation.

Keywords : sea ice, AMSR-E, ice concentration

1. Introduction

The Advanced Microwave Scanning Radiometer for EOS (AMSR-E) developed and built by the Japan Aerospace Exploration Agency for NASA was successfully launched on the EOS Aqua spacecraft in May 2002. This new state-of-the-art satellite radiometer provides a wider range of frequencies and twice the spatial resolution than is currently available with the Defense Meteorological Satellite Program (DMSP) Special Sensor Microwave/Imager (SSM/I) series of radiometers (see Kawanishi et al.[1] for a summary of AMSR-E frequencies, beamwidths, and mean spatial resolutions. The resolution of the AMSR-E is increased by roughly a factor of two compared to the SSM/I. The resolution of the 19 to 89 GHz channels range from 25 to 5 km.

Sea ice concentrations for the U.S. Aqua AMSR-E sea ice product suite are operationally calculated using an enhanced version of the NASA Team (NT) algorithm[2], henceforth referred to as NT2 algorithm. This algorithm was originally developed for the Special Sensor Microwave Imager (SSM/I) on board the U.S. Defense Meteorological Satellite Program (DMSP) satellites. The enhancement to the NT algorithm is achieved mainly through the incorporation of the 89 GHz channels (85 GHz for the SSM/I), while retaining both the relative insensitivity to ice temperature variations that the use

of radiance ratios provide and the relatively large dynamic range in sea ice concentration that the use of the 19 and 37 GHz channels provide. Mätzler et al.[3] have shown that the sensitivity to inhomogeneities of the surface layer on the horizontal polarization at 85 GHz is much reduced and therefore have suggested the use of the 85 GHz channels for ice concentration retrievals if one can handle its higher sensitivity to atmospheric effects compared to the 19 GHz and 37 GHz channels. For the AMSR-E NT2 algorithm the higher sensitivity to atmospheric effects at 89 GHz is handled through forward calculations with a full atmospheric radiative transfer model[4]. There exist other studies that investigated the use of the 85-GHz channels to derive ice concentrations at a higher spatial resolution. Svendsen et al.[5] and Lubin et al.[6] used the 85-GHz data with a simplified radiative transfer model. They obtained good results when cloud contamination was small[6]. Others used the 85-GHz data in successive combination with the low frequency channels to retrieve high resolution ice concentration[7,8], or a combination of 85 GHz data with model results from numerical weather predictions[9].

This paper provides an overview of the theoretical basis of the NT2 algorithm and then gives some details on the implementation of the algorithm by the U.S. AMSR-E Science Team. Included in this overview is a description of the reduction of atmospheric effects, the removal of erroneous sea ice concentrations near the coast that result from the large

AMSR-E antenna pattern and a summary of recent validation results. The algorithm look-up tables needed for implementation of the algorithm are given in the appendix.

2. Heritage

The two ratios of brightness temperatures used in the original NT algorithm as well as in the NT2 approach are the polarization

$$PR(\nu) = \frac{TB(\nu V) - TB(\nu H)}{TB(\nu V) + TB(\nu H)} \qquad (1)$$

and the spectral gradient ratio

$$GR(\nu_1 p \nu_2 p) = \frac{TB(\nu_1 p) - TB(\nu_2 p)}{TB(\nu_1 p) + TB(\nu_2 p)} \qquad (2)$$

where TB is the brightness temperature at frequency ν for the polarized component p (vertical (V) or horizontal (H)).

Figure 1a shows a typical scatterplot of PR (19) versus GR (37V19V) for September conditions in the Weddell Sea. The NT algorithm identifies two ice types which are associated with first-year and multiyear ice in the Arctic and ice types A and B in the Antarctic (as shown in Figure 1a). The A-B line represents 100% ice concentration. The distance from the open water point (OW) to line A-B is a measure of the ice concentration. In this algorithm, the primary source of error is attributed to conditions in the surface layer such as surface glaze and layering[10], which can significantly affect the horizontally polarized 19 GHz brightness temperature[3] leading to increased PR (19) values and thus an underestimate of ice

concentration. In the following discussion, we will refer to these effects as surface effects. In Figure 1a, pixels with significant surface effects tend to cluster as a cloud of points towards higher PR values (labeled C) away from the 100% ice concentration line A-B resulting in an underestimate of ice concentration by the NT algorithm. The use of horizontally polarized channels makes it imperative to resolve a third ice type to overcome the difficulty of surface effects on the emissivity of the horizontally polarized component of the brightness temperature.

3. Theoretical Basis

We make use of GR (89V19V) and GR (89H19H) to resolve the ambiguity between pixels with true low ice concentration and pixels with significant surface effects. A plot of these two ratios are found to form narrow clusters except for areas where surface effects result in a decrease in TB (19H) and thus an increase in GR (89H19H) (Figure 1b). Values of high GR (89V19V) and high GR (89H19H) are indicative of open water. The range of GR (89H19H) values is larger because of the greater dynamic range between ice and water for the horizontally polarized components. With increasing ice concentration, the two ratios have more similar values. The narrow cluster of pixels adjacent to the diagonal shown in Figure 1b represents 100% ice concentration with different GR values corresponding to different ice types. When surface effects come into play, points deviate from this narrow cluster towards increased GR (89H19H) values (cloud of points to the right of the diagonal) while GR (89V19V) changes little or
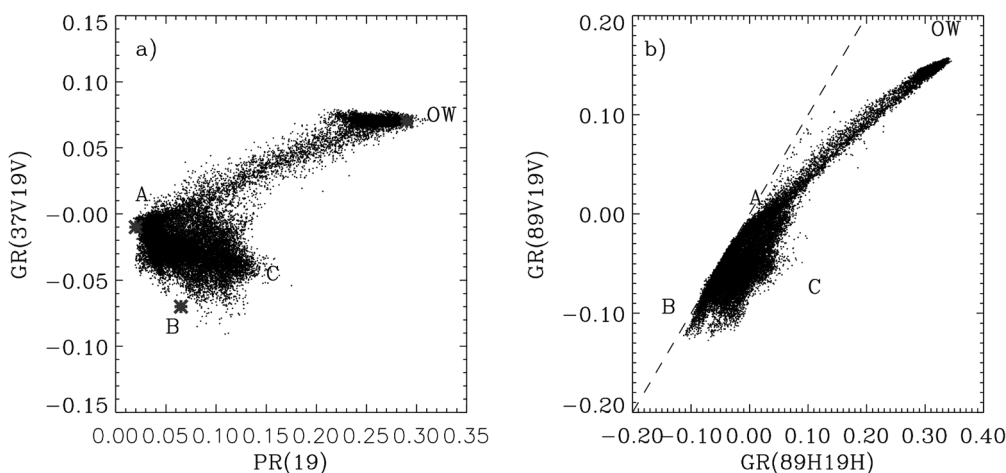

Fig. 1 a) GR (37V19V) versus PR (19) for the Weddell Sea on September 15, 2008. The gray symbols represent the tiepoints for the ice types A and B as well as for open water as used by the NT algorithm. Label C indicates pixels with significant surface effects. ϕ is the angle between the y-axis and the A-B line. b) GR (85V19V) versus GR (85H19H). The ice types A and B are close to the diagonal (dahsed line). The amount of layering corresponds to the horizontal deviation from this line towards label C. Adapted from Markus and Cavalieri[2].
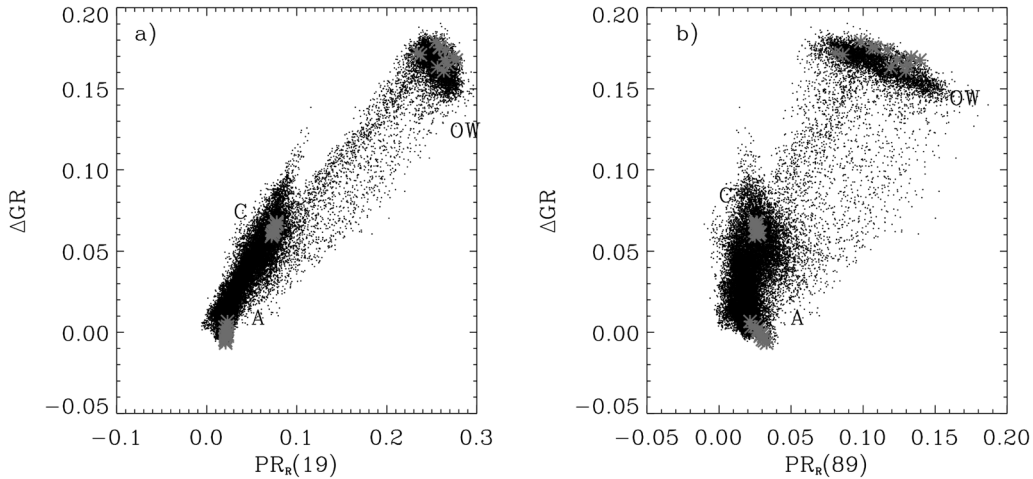
Fig. 2　$\triangle GR$ over $PR(19)_R$ (a) and $\triangle GR$ over $PR(89)_R$ (b) for September 15, 2008. They gray symbols represent the NT2 tiepoints.

remains constant. This cloud of points labeled C in Figure 1 b also corresponds to the cluster of points labeled C in Figure 1a. Therefore. the difference between these two GRs ($\triangle GR$) is used as a measure of the magnitude of surface effects. Based on this analysis we introduce a new ice type C which represents ice having significant surface effects. For computational reasons we rotate the axes in PR-GR space (Figure 1a) by an angle ϕ so the A-B line is vertical. This makes the rotated PR_S ($PR_R(19)$ and $PR_R(89)$) independent of ice types A and B (first-year and multiyear ice for the Arctic) and effectively eliminates one ice type in the ice concentration calculations. In the following ice type A will be the combination of ice types A and B (or first-year and multiyear for the Arctic). The addition of the 89 GHz data in the algorithm requires a correction for atmospheric effects. This is accomplished through an additional AMSR-E variable, the polarization at 89 GHz ($PR(89)$).

The response of the brightness temperatures to different weather conditions is quantified using an atmospheric radiative transfer model[4]. Input data into the model are the emissivities of first-year sea ice under winter conditions taken from Eppler et al.[11] with modifications to achieve agreement between modeled and observed ratios. Atmospheric profiles, used as another independent variable in the algorithm, having different cloud properties, specifically cloud base, cloud top, cloud liquid water are taken from Fraser et al.[12] and average atmospheric temperatures and humidity profiles for summer and winter conditions are taken from Antarctic research stations. These atmospheric profiles are based on climatology and are assumed valid for both hemispheres.

The plots of $\triangle GR$ versus $PR_R(19)$ (Figure 2a) and $\triangle GR$ versus $PR_R(89)$ (Figure 2b) illustrate the algorithm domain. The gray symbols indicate the tiepoints with the different

atmospheres for the three surface types (A, C, and OW). They also illustrate that the effect of weather is well modeled. For example, the cluster of open water is mainly a result of changing atmospheric conditions. The modeled atmospheres adequately span the lengths of the OW clusters. A comparison of Figures 2a and 2b also shows how much more the 89 GHz data are affected by the atmosphere compared to the 19 GHz data.

We then calculate brightness temperatures for all possible ice concentration combinations in 1% increments and for each of those solutions calculate the ratios $PR_R(19)$, $PR_R(89)$, and $\triangle GR$. This creates a prism in which each element contains a vector with the three ratios. For each AMSR-E pixel $PR_R(19)$, $PR_R(89)$, and $\triangle GR$ are calculated from the observed brightness temperatures. Next, we move through this prism comparing the observed three ratios with the modeled ones. The indices where the differences are smallest determines the final ice concentration combination and weather index. The next section will provide detailed information about the implementation.

Because of the unique signature of new ice in the microwave range we solve for new ice instead of ice type C for selected pixels. Using a $GR(37V19V)$ threshold of -0.02 we either resolve ice type C (for pixels where $GR(37V19V)$ is below this threshold) or new ice (for pixels where $GR(37V19V)$ is above this threshold). Areas of ice type C and new ice are mutually exclusive because new ice has little, if any, snow cover. A limitation, of course, is that we cannot resolve mixtures of new ice and thicker ice with layering in its snow cover.

4. Implementation

4.1　Calculation of ice concentrations
In contrast to other operational sea ice concentration algo-

rithms using daily averaged brightness temperatures as input, the AMSR-E NT2 concentrations are calculated from individual swath (Level 2) data from which daily maps are made by averaging these swath ice concentrations. Using swath brightness temperatures is particularly critical for the NT2 algorithm and its atmospheric correction. The atmospheric influence on the brightness temperatures is non linear and by using average brightness temperatures we would dilute the atmospheric signal.

The ice concentration algorithm is implemented as follows :

1.   Generate look-up tables : For each AMSR channel with frequency ν and polarization p calculate brightness temperature for each ice concentration-weather combination (using TB_{ow}, TB_A, TB_C as given in the appendix) :

$$TB_{C_A, C_C, W_x}(\nu p) = (1 - C_A - C_C) \times TB_{ow}(\nu p W_x) + C_A \times TB_A(\nu p W_x) + C_C \times TB_C(\nu p W_x) \tag{3}$$

where C_A refers to the combined concentration of ice types A and B for the Antarctic and first-year andmultiyear ice for the Arctic (because of the axis rotation), C_C to ice type C concentration, and W_x to the weather index. As mentioned above, for pixels where $GR\,(37V19V) > -0.02$ C_C and TB_C will represent new ice. Ice concentrations are between 0 and 100 in 1% increments, weather indices are between 1 and 12 corresponding to the tables in the Appendix.

2.   From these TBs calculate ratios creating the look-up tables, e.g. $LUT_{PR19}\,(ca,\,cc,\,w_x)$ etc. :

$$LUT_{PR19}(c_C, c_C, w_x) =$$
$$\frac{TB_{C_A, c_C, w_x}(37V) - TB_{C_A, c_C, w_x}(19V)}{TB_{C_A, c_C, w_x}(37V) + TB_{C_A, c_C, w_x}(19V)} \sin\phi_{19}$$
$$+ \frac{TB_{C_A, c_C, w_x}(19V) - TB_{C_A, c_C, w_x}(19H)}{TB_{C_A, c_C, w_x}(19V) + TB_{C_A, c_C, w_x}(19H)} \cos\phi_{19} \tag{4}$$

$$LUT_{PR89}(c_A, c_C, w_x) =$$
$$\frac{TB_{C_A, c_C, w_x}(37V) - TB_{C_A, c_C, w_x}(19V)}{TB_{c_A, c_C, w_x}(37V) + TB_{C_A, c_C, w_x}(19V)} \sin\phi_{89}$$
$$+ \frac{TB_{C_A, c_C, w_x}(89V) - TB_{C_A, c_C, w_x}(89H)}{TB_{C_A, c_C, w_x}(89V) + TB_{C_A, c_C, w_x}(89H)} \cos\phi_{89} \tag{5}$$

If $GR\,(37V19V) \leq -0.02$ we resolve for ice type C using ΔGR as our third variable, i.e.,

$$LUT_{\Delta GR}(c_A, c_C, w_x) =$$
$$\frac{TB_{C_A, c_C, w_x}(89H) - TB_{C_A, c_C, w_x}(19H)}{TB_{C_A, c_C, w_x}(89H) + TB_{c_A, c_C, w_x}(19H)}$$
$$- \frac{TB_{C_A, c_C, w_x}(89V) - TB_{C_A, c_C, w_x}(19V)}{TB_{C_A, c_C, w_x}(89V) + TB_{C_A, c_C, w_x}(19V)} \tag{6}$$

whereas for pixels where $GR\,(37V19V) > -0.02$ we resolve for new ice using the standard $GR\,(37V19V)$ as suggested by Cavalieri[13], i.e.

$$LUT_{\Delta GR}(C_A, C_C, W_x) =$$
$$\frac{TB_{C_A, c_C, W_x}(37V) - TB_{C_A, c_C, W_x}(19V)}{TB_{C_A, c_C, W_x}(37V) + TB_{C_A, c_C, W_x}(19V)} \tag{7}$$

Each of these arrays has the dimensions of $101 \times 101 \times 12$ where, of course, the total ice concentration $(C_A + C_C)$ cannot exceed 100.

3.   For each pixel i we have the actual measured AMSR-E brightness temperatures $(TB_i\,(\nu p))$

4.   Calculate same ratios from these brightness temperatures as in step 2 $(PR_i\,(19)$, etc.).

5.   Compare these observed ratios with each of the ratios in the look-up tables looping through all ice concentration-weather combinations, i.e.

$$\delta = (PR_i(19) - LUT_{PR19}(C_A, C_C, W_x))^2 + (PR_i(89) - LUT_{PR89}(C_A, C_C, W_x))^2 + (\Delta GR_i - LUT_{\Delta GR}(C_A, C_C, W_x))^2 \tag{8}$$

6.   The indices ca, cc, wx where δ is minimal determine the ice concentration (and weather index), i.e.

$$C_T = C_{A min\delta} + C_{C min\delta} \tag{9}$$

4.2   Land spillover correction

Although a land mask is applied to the ice concentration maps, land spillover still leads to erroneous ice concentrations along the coast lines. This makes operational usage of these maps cumbersome. Therefore, we apply a land spillover correction scheme on the maps. The difficulty is to delete all clearly erroneous ice concentration while at the same time preserving actual ice concentrations, as for example, along the margins of coastal polynyas. We apply a five step procedure :

1.   Classify all pixels of the polar-stereographic grid with respect to their distance to coast (Figure 3).

2.   All pixels with classes 1 or 2 will be assessed for erroneous sea ice concentrations due to land spillover by analyzing the 7 by 7 pixel neighborhood. The area of the neighborhood (7 pixels or 87.5 km) needs to be greater than the AMSR-E antenna pattern. Pixels with values of 3 and 0 will not be changed.

3.   Check whether all class 3 pixels in 7 pixel neighborhood are open water (if so, set ice concentration to 0).

4.   Calculate an average sea ice concentration for the 7 by 7 pixel box assuming all ocean pixels have zero ice concentration and all land pixels have an ice concentration of 90%. This approximates a theoretical concentration caused by land spillover only.

5. If the AMSR-E ice concentration is less or equal this value set pixel at center of box to open water.

Figure 4 shows an ice concentration map with and without the land spillover correction.

4.3 Reduction of atmospheric effects

As explained above, the NT2 algorithm has an atmospheric correction scheme as an inherent part of the algorithm. It provides weather-corrected sea ice concentrations through the utilization of a forward atmospheric radiative transfer model. However, to eliminate remaining severe weather effects over open ocean, two weather filters based on the spectral gradient ratio are implemented using threshold values similar to those used by the NT algorithm[14)15)]. However, the advantage of

```
0  3  2  1 |4  4  4  4  5  6  7  7  7  7  7  7  7  7  7  7
0  3  2  1 |4  5  5  5  6  7  7  7  7  7  7  7  7  7  7  7
0  3  2  1 |4  5  6  6  6  6  7  7  7  7  7  7  7  7  7  7
0  3  2  1 |4  4  5  5  5  5  6  7  7  6  6  6  7  7  7
0  3  2  1 |1  4  4  4  4  4  5  6  6  5  5  5  6  7  7
0  0  3  2  1  1 |1 |4 |1  4  5  5  5  4  4  5  6  7
0  0  0  3  2  2  1  1 |4  4  4  4  4 |1 |4  5  6  7
0  0  0  0  3  3  2  2  1  1  1  1 |4 |1  1  4  4  5  6
0  0  0  0  0  0  3  3  2  2  2  2  1  1  1 |1  4  4  5
0  0  0  0  0  0  0  3  3  3  3  2  2  2  1 |1 |4  4
0  0  0  0  0  0  0  0  0  3  3  3  3  2  1 |1 |1
0  0  0  0  0  0  0  0  0  0  0  0  0  0  3  2  2  2
0  0  0  0  0  0  0  0  0  0  0  0  0  0  0  3  3  2
```
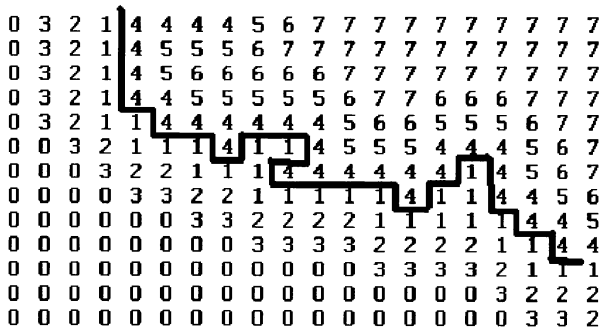
Fig. 3 Example coastline classification map. Ocean pixels directly along the coast are classified with 1, pixels farther away are 2 and 3. Open ocean pixels are zero. Land pixels directly along the coast are classified as 4 and pixels farther away have increasing values.

the radiative transfer atmospheric correction is that not only are spurious ice concentrations in the open ocean removed, but atmospheric corrections are applied to ice covered portions of the ocean.

Figure 5 shows an example for the Sea of Okhotsk. Figure 5a shows the ice concentrations if PR_R (19), PR_R (89), and ΔGR are used but without any weather correction. Figure 5b shows the ice concentration with the NT2 weather correction. The differences between those two concentrations (Figure 5d) illustrate the effect of the weather correction not only over the open ocean but also over the sea ice. More severe weather effects over the open ocean (for example, in the bottom right corner) are finally removed by the NT weather filter (Figure 5c). The threshold of this weather filter (pixels where GR (37 $V19V$) >0.05 or GR (22$V19V$) >0.045 are set to 0% ice concentration) sets ice concentrations of less than 15% to 0% therefore we also observe a slight change along the sea ice edge (Figure 5e).

Even with both the atmospheric correction scheme and the GR filters, we still can have problems with residual weather contamination particularly at lower latitudes. A filter based on monthly climatological sea surface temperatures (SSTs) from the National Oceanic and Atmospheric Administration (NOAA) ocean atlas used earlier[16)] was employed to eliminate these low-latitude spurious ice concentrations. In the Northern Hemisphere, in any pixel where the monthly SST is greater than 278 K, the ice concentration is set to zero throughout the month ; whereas in the Southern Hemisphere,

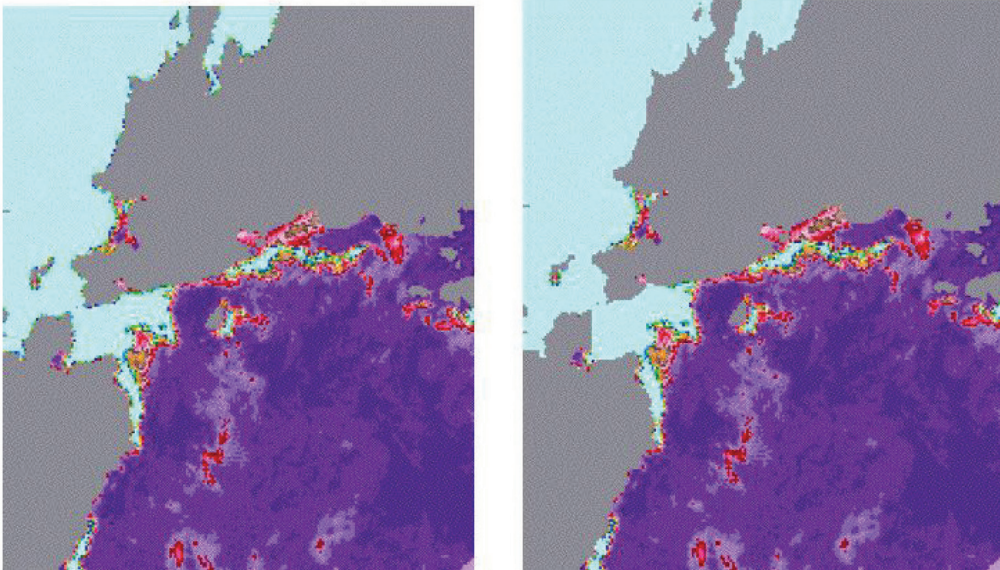without land spillover correction   with land spillover correction

Fig. 4 Map of ice concentration with and without land spillover correction.
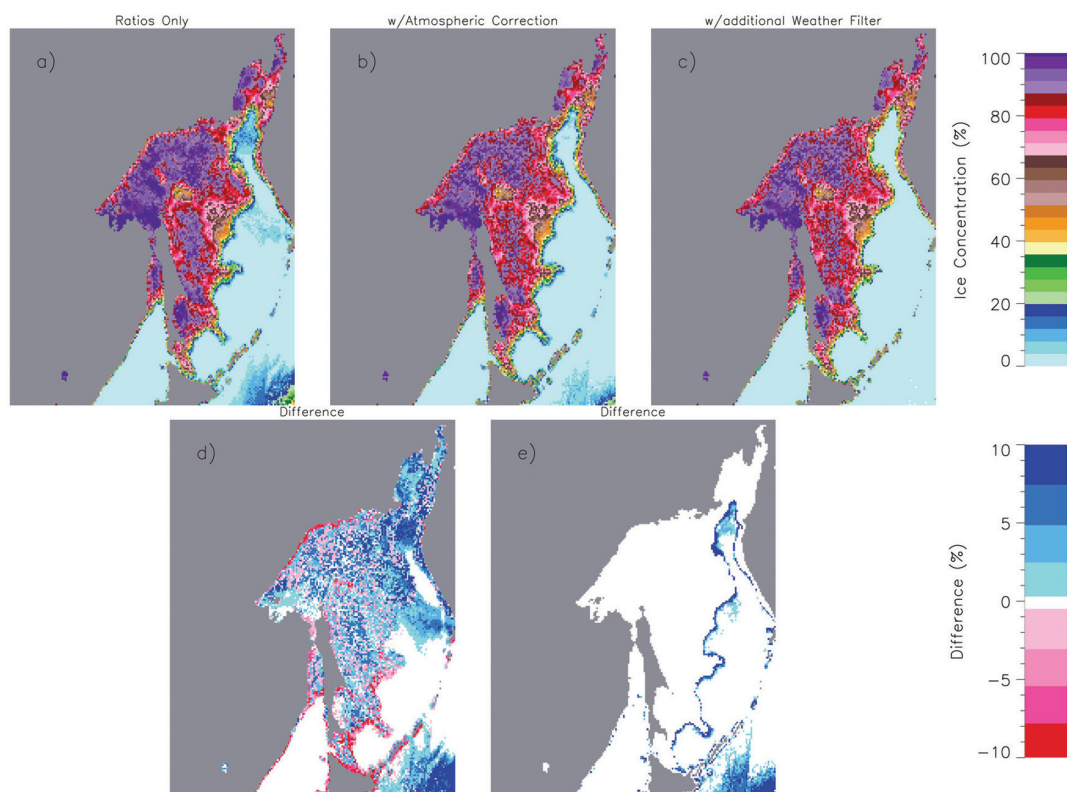
Fig. 5　AMSR-E sea ice concentrations for March 1, 2007.　(a) Ice concentrations calculated using PR_R (19), PR_R (89), ΔGR without applying an atmospheric correction ; (b) ice concentration with atmospheric correction ; (c) final ice concentration with additional clean-up over the open ocean by applying the standard NASA Team GR weather filter. (d) difference between (a) and (b). (e) difference between (b) and (c).　Differences greater than 10% have been truncated for the erroneous sea ice concentrations in the lower right corner.

wherever the monthly SST is greater than 275 K, the ice concentration is set to zero throughout the month.　The higher SST threshold value in the Northern Hemisphere is needed because the 275 K isotherm used in the South is too close to the ice edge in the North.　The closest distance the threshold isotherms are to the ice edge is more than 400 km[16].

In summary, the order of the processing is as follows :

1. Calculate sea ice concentrations with atmospheric correction.
2. Apply GR weather filters.
3. Apply SST mask
4. Apply land spill over correction.

5.　Validation

Several studies exist that evaluate the performance of the NT2 algorithm and, in some studies, compare its results with results from other algorithms.　The first comparison of NT2 retrievals with those from other algorithms is presented in the NT2 algorithm paper[2].　In this paper the authors compared sea ice concentrations derived from AVHRR imagery with those obtained from the NT, NT2, and Bootstrap (BS)[17] sea

ice algorithms for transects both across the Ross Sea and the Sea of Okhotsk.　For both transects, the NT2 algorithm had the highest correlation and the smallest bias relative to the AVHRR ice concentrations.

Markus and Dokken[18] investigated the algorithm's performance in the Arctic during late summer through the comparison with RADARSAT and ERS SAR ice concentrations obtained using an automated SAR ice discrimination algorithm.　Two study regions were examined.　The first was located within the Arctic ice pack where ice concentrations ranged from 60% to 100%.　The correlation between the NT 2 and SAR concentrations was 0.87 with little bias (-0.2%).　The second region was located within the marginal ice zone where the agreement was not as good.　The correlation was 0.66 with a bias toward higher SAR concentrations.　Nonetheless, the NT2 algorithm outperformed the NT algorithm which significantly underestimated ice concentations relative to SAR.

McKenna et al.[19] compared several algorithms including the NT, the BS, and the NT2 algorithms with ice charts from the U.S. National Ice Center (NIC).　The NIC ice charts are primarily based on high resolution visible and infrared image-

ry from both civilian and defense department satellites, but use passive microwave satellite imagery under cloudy conditions. A total of 13 comparative studies were completed. They found that the NT2 algorithm overwhelmingly outperformed the other algorithms and provided consistently better estimates of the ice edge and the 90% ice concentration boundary.

Meier[20] undertook a more comprehensive study comparing Arctic ice concentrations from the NT, BS, and NT2 algorithms with AVHRR derived ice concentrations. The regions of study included Baffin Bay, the Greenland Sea, and the Kara and Barents seas. His results show that the NT2 algorithm has the smallest mean difference for all pixels during both summer and winter seasons separately, although all three algorithms tend to underestimate ice concentration during summer relative to AVHRR.

Cavalieri et al.[21] undertook a comparison between AMSR-E NT2 Arctic sea ice concentrations and Landsat 7 Enhanced Thematic Mapper Plus imagery obtained during March 2003. Good overall agreement was obtained with little bias (1%) for areas of first year and young sea ice. However, in areas of new ice production there was a negative bias of about 5% in the AMSR-E ice concentration retrievals, with a root mean square error of 8%. Some areas of deep snow were also found to result in an underestimate of the ice concentration (10%). However, for all ice types combined and for the full range of ice concentrations, the bias ranged from 0% to 3%, and the rms errors ranged from 1% to 7%, depending on the region. Since these results were reported, the new ice tie-points have been adjusted which should reduce the low concentration bias.

Massom et al.[22] compared the NT2 algorithm and the AMSR-E Bootstrap algorithm with aerial photography in East Antarctica. They found very similar ice concentrations for the two AMSR-E ice concentrations with small overestimation compared to the aerial photography.

Andersen et al.[23] compared seven passive microwave sea ice concentration algorithms (among them the NT2) with ship-based observations and SAR-based concentrations. Algorithms which use 85 GHz information consistently had the best agreement with both SAR ice concentrations and ship observations. They furthermore found that the greater atmospheric contribution in the 89 GHz data is not as important as variabilities in surface emissivity.

6. Summary

This paper provides an overview of the physical basis and implementation of the NT2 sea ice concentration algorithm used by the U.S. AMSR-E Science Team for its standard sea ice products. The NT2 algorithm incorporates both features of the NT heritage algorithm and new enhancements including a radiative transfer model to provide an atmospheric correction to the retreivals. Several comparative studies have shown that the algorithm provides stable and reliable sea ice concentrations for both hemispheres. The processing code also includes weather filters for eliminating spurious weather effects over open ocean, sea surface temperature masks for eliminating residual weather effects particularly at low latitudes, and a correction for eliminating spurious sea ice concentrations along the coast as a result of the broad AMSR-E antenna pattern.

References

1) T. Kawanishi, T. Sezai, Y. Ito, K. Imaoka, T. Takeshima, Y. Ishido, A. Shibata, M. Miura, H. Inahata and R. W. Spencer : The Advanced Microwave Scanning Radiometer for the Earth Observing System (AMSR-E), NASDA's contribution to the EOS global energy and water cycle studies, IEEE Trans. Geoscience Rem. Sens., 41, pp. 184–194, 2003.

2) T. Markus and D. J. Cavalieri : An enhancement of the NASA Team sea ice algorithm, IEEE Trans. Geoscience Remote Sensing, 38, pp. 1387–1398, 2000.

3) C. Mätzler, R. O. Ramseier, and E. Svendsen : Polarization effects in sea-ice signatures, IEEE J. Oceanic Eng., OE-9, pp. 333–338, 1984.

4) C. Kummerow : On the accuracy of the Eddington approximation for radiative transfer in the microwave frequencies, J. Geophys. Res., 98, pp. 2757–2765, 1993.

5) E. Svendsen, C. Matzler and T. C. Grenfell : A model for retrieving total sea ice concentration from a spaceborne dual-polarized passive microwave instrument operating at 90 GHz, Int. J. Remote Sensing, 8, pp.1479–1487, 1987.

6) D. Lubin, C. Garrity, R. O. Ramseier, and R. H. Whritner : Total sea ice concentration retrieval from the SSM/I 85.5 GHz channels during the Arctic summer, Remote Sens. Environ., vol. 62, pp. 63–76, 1997.

7) K. M. St. Germain : A two-phase algorithm to correct for atmospheric effects on the 85 GHz channels of the SSM/I in the Arctic region, Proc. International Geoscience and Remote Sensing Symposium, Pasadena, CA, pp. 148–151, 1994.

8) L. Kaleschke, C. Luepkes, T. Vihma, J. Haarpainter, A. Bochert, J. Hartmann and G. Heygster : SSM/I sea ice remote sensing for mesoscale ocean-atmosphere interaction analysis,

Canadian Journal of Remote Sensing, 27, pp. 526–537, 2001.

9）S. Kern : A new method for medium-resolution sea ice analysis using weather-influence corrected Special Sensor Microwave/Imager 85 GHz data, Int. J. Remote Sensing, 25, pp. 4555–4582, 2004.

10）J. C. Comiso, D. J. Cavalieri, C. L. Parkinson and P. Gloersen : Passive microwave algorithms for sea ice concentration—A comparison of two techniques, Remote Sens. Environ., 60, pp. 357–384, 1997.

11）D.T. Eppler and 14 others : Passive microwave signatures of sea ice, in Microwave Remote Sensing of Ice, Geophys. Monogr. Ser., vol. 68, F. Carsey (ed.), pp. 47–71, AGU, Washington, D. C., 1992.

12）R. S. Fraser, N. E. Gaut, E. C. Reifenstein and H. Sievering : Interaction Mechanisms—Within the Atmosphere, in Manual of Remote Sensing, R. G. Reeves, A. Anson, D. Landen (eds.), pp. 181–233, American Society of Photogrammetry, Falls Church, VA, 1975.

13）D. J. Cavalieri : A microwave technique for mapping thin sea ice. J. Geophys. Res., 104, 12,561–12,572, 1994.

14）P. Gloersen and D. J. Cavalieri : Reduction of weather effects in the calculation of sea ice concentration from microwave radiances, J. Geophys. Res., 91, pp. 3913–3919, 1986.

15）D. J. Cavalieri, K. St. Germain and C. T. Swift : Reduction of Weather Effects in the Calculation of Sea Ice Concentration with the DMSP SSM/I, J. Glaciology, 41, pp. 455–464, 1995.

16）D. J. Cavalieri, C. L. Parkinson, P. Gloersen, J. C. Comiso and H. J. Zwally : Deriving Long-Term Time Series of Sea Ice Cover from Satellite Passive-Microwave Multisensor Data Sets, J. Geophys. Res., 104, pp. 15,803–15,814, 1999.

17）J. C. Comiso : SSM/I sea ice concentrations using the bootstrap algorithm, NASA Reference Publication, 1380, 49 pp., 1995.

18）T. Markus and S. T. Dokken : Evaluation of Arctic late summer passive microwave sea ice retrievals, IEEE Trans. Geoscience Remote Sensing, 40, pp. 348–356, 2002.

19）P. McKenna, W. N. Meier, M. L. van Woert, M. Chase and K. Dedrick : SSM/I Sea Ice Algorithm Inter-Comparison : Operational Case Studies from the National Ice Center, Proc. International Geoscience and Remote Sensing Symposium, Toronto, Canada, 2002.

20）W. Meier : SSM/I sea ice concentrations in the marginal ice zone : A comparison of four algorithms with AVHRR imagery, IEEE Trans. Geosci. and Rem. Sensing, 43, pp. 1324–1337, 2005.

21）D. J. Cavalieri, T. Markus, D. K. Hall, A. Gasiewski, M. Klein and A. Ivanoff : Assessment of EOS Aqua AMSR-E Arctic sea ice concentrations using airborne microwave and Landsat 7 imagery, IEEE Trans. Geoscience Rem. Sens., 44, 3057–3069, 2006.

22）R. A. Massom, A. Worby, V. Lytle, T. Markus, I. Allison, T. Scambos, H. Enomoto, K. Tateyama, T. Haran, J. C. Comiso, A. Pfaffling, T. Tamura, A. Muto, P. Kanagaratnam, B. Giles, N. Young, G. Hyland and E. Key : ARISE (Antarctic Remote Ice Sensing Experiment) in the East 2003 : validation of satellite-derived sea-ice data products, Ann. Glaciol. 44, pp. 288–296, 2006.

23）S. Andersen, R. Tonboe, L. Kaleschke, G. Heygster and L. T. Pedersen : Intercomparison of passive microwave sea ice concentration retrievals over the high-concentration Arctic sea ice, J. Geophys. Res., 112, doi : 10.1029/2006JC003543, 2007.

Appendices : Look-up tables for AMSR-E

Table 1　Open water ; Arctic and Antarctic

Wx index	19H	19V	22V	37H	37V	89H	89V
1	99.4	184.5	196.7	132.3	211.9	181.9	248.8
2	96.0	181.3	192.1	129.4	208.7	171.6	243.6
3	103.8	186.5	199.2	140.3	214.7	190.2	249.3
4	100.9	183.5	194.5	136.6	211.0	178.0	243.9
5	100.8	185.2	197.7	134.8	212.9	188.0	250.1
6	97.2	181.9	192.9	132.0	209.7	176.4	244.5
7	103.6	186.6	199.6	142.4	216.1	202.5	253.1
8	101.1	183.8	195.4	141.0	213.2	190.4	246.8
9	106.0	187.8	201.2	148.4	218.5	212.5	255.2
10	104.3	185.3	197.4	148.1	216.0	200.1	248.4
11	115.1	192.1	206.7	165.9	225.0	227.2	255.6
12	113.2	189.6	202.8	164.5	222.2	218.0	250.5

Table 3　New ice C ; Arctic and Antarctic

Wx index	19H	19V	22V	37H	37V	89H	89V
1	173.9	239.2	239.5	192.1	242.9	209.1	248.4
2	160.1	221.3	221.3	178.3	225.3	190.1	229.7
3	176.1	239.6	240.1	196.1	243.5	214.1	248.7
4	162.8	221.9	222.1	182.2	226.1	194.4	230.4
5	174.6	239.4	239.9	193.5	243.3	213.1	249.6
6	160.8	221.5	221.7	179.8	225.8	193.6	230.8
7	176.2	239.9	240.6	197.7	244.6	222.7	252.3
8	163.1	222.2	222.8	185.0	227.6	203.5	234.1
9	177.5	240.2	241.2	201.0	245.6	229.3	254.2
10	164.9	222.8	223.6	189.0	229.0	210.5	236.5
11	182.3	241.3	242.8	209.9	247.4	238.0	254.5
12	169.9	224.4	226.0	198.4	232.0	223.4	240.4

Table 2　Ice type A (first-year and multiyear for Arctic) ;
　　　　　Arctic and Antarctic

Wx index	19H	19V	22V	37H	37V	89H	89V
1	243.7	257.9	258.4	242.8	257.2	230.1	242.7
2	224.9	238.8	239.6	224.3	239.1	209.8	225.4
3	243.9	257.7	258.2	243.5	257.1	233.0	243.8
4	225.3	238.7	239.6	225.3	239.1	212.4	226.7
5	243.8	258.0	258.5	243.3	257.5	232.8	244.2
6	225.1	238.9	239.7	224.9	239.3	212.1	226.8
7	244.2	258.1	258.7	244.8	258.1	239.3	247.8
8	225.7	239.1	240.1	226.9	240.3	219.2	230.9
9	244.5	258.2	258.8	245.8	258.6	243.9	250.4
10	226.2	239.3	240.4	228.5	241.0	224.1	233.8
11	245.3	258.2	258.8	248.2	258.8	248.8	252.3
12	227.6	239.9	241.2	232.0	242.6	233.2	239.0

Table 4　Ice type C ; Arctic

Wx index	19H	19V	22V	37H	37V	89H	89V
1	190.0	236.2	233.9	190.1	225.4	195.5	219.6
2	175.2	218.5	215.9	176.4	209.1	176.4	200.7
3	191.7	236.7	234.7	194.3	227.1	202.0	223.4
4	177.3	219.2	216.9	180.4	211.0	181.9	204.0
5	190.6	236.4	234.3	191.5	226.1	200.4	222.9
6	175.8	218.7	216.3	178.0	209.9	180.6	203.5
7	191.9	237.0	235.2	195.8	228.4	212.4	230.6
8	177.6	219.5	217.6	183.3	212.9	192.9	211.7
9	193.0	237.4	235.9	199.2	230.2	220.7	236.0
10	179.2	220.2	218.7	187.4	215.2	201.5	217.4
11	196.8	238.6	238.0	208.4	234.5	232.2	242.4
12	183.3	221.9	221.5	197.1	220.4	217.5	228.0

Table 5   Ice type C; Antarctic

Wx index	19H	19V	22V	37H	37V	89H	89V
1	187.2	227.6	231.6	190.3	221.9	211.6	227.6
2	171.9	210.4	214.9	176.5	205.9	196.6	210.2
3	189.1	228.4	232.4	194.3	223.9	215.3	230.5
4	174.1	211.5	216.0	180.4	207.9	199.7	212.8
5	187.9	227.9	232.0	191.7	222.7	214.6	230.1
6	172.5	210.8	215.4	178.0	206.8	199.2	212.5
7	189.3	228.7	232.9	195.9	225.2	221.7	236.5
8	174.6	211.9	216.6	183.3	210.0	206.6	219.2
9	190.6	229.3	233.5	199.3	227.1	226.7	240.9
10	176.2	212.7	217.5	187.4	212.4	211.8	223.9
11	194.8	231.1	235.6	208.3	231.9	233.3	246.0
12	180.8	215.1	220.3	196.9	218.0	221.6	232.6

● **Thorsten Markus**

Thorsten Markus received the M.S. and Ph. D. degrees in physics from the University of Bremen, Bremen, Germany, in 1992 and 1995, respectively. He was a National Research Council Resident Research Associate with the Goddard Space Flight Center (GSFC) from 1995 to 1996 before joining the NASA‒University of Maryland Baltimore County (UMBC) Joint Center for Earth Systems Technology, UMBC, Baltimore, where he worked until 2002. He is currently the Head of the Cryospheric Sciences Branch in the Hydrospheric and Biospheric Sciences Laboratory, NASA GSFC, Greenbelt, MD. His research interests include satellite remote sensing, and the utilization of satellite data to study cryospheric, oceanic, and atmospheric processes.
E-mail : Thorsten.Markus@nasa.gov

● **Donald J. Cavalieri**

Donald J. Cavalieri received the B.S. degree in physics from the City College of New York, New York, in 1964, the M.A. degree in physics from Queens College, New York, in 1967, and the Ph.D. degree in meteorology and oceanography from New York University, New York, in 1974. From 1974 to 1976, he was a National Research Council Postdoctoral Resident Research Associate with the National Oceanic and Atmospheric Administrationyq Environmental Data Service, Boulder, CO, where he continued his doctoral research on stratospheric-ionospheric coupling. From 1976 to 1977, he was a Visiting Assistant Professor with the Department of Physics and Atmospheric Science, Drexel University, Philadelphia, PA, where he worked on stratospheric temperature retrievals from satellite infrared radiometers. In the fall of 1977, he was a Staff Scientist with Systems and Applied Sciences Corporation, Riverdale, MD, where he worked on sea ice retrieval algorithms, in preparation for the launch of Nimbus-7 SMMR. In 1979, he joined the Laboratory for Atmospheres, NASA Goddard Space Flight Center, Greenbelt, MD, where he is currently a Senior Research Scientist with the Cryospheric Sciences Branch, Hydrospheric and Biospheric Sciences Laboratory. His current research interests include polar ocean processes and microwave remote sensing of the cryosphere.
E-mail : Donald.J.Cavalieri@nasa.gov